# Event Detection and Characterization in Continuous Recording of Synchro-waveforms: Field Experiments and Data Analytics

Narges Ehsani, Fatemeh Ahmadi-Gorjayi, Zong-Jhen Ye, Alex McEachern, and Hamed Mohsenian-Rad

***Abstract*— This paper presents a novel practical and theoretical foundation for detecting and characterizing events in continuously recorded, time-synchronized voltage waveform measurements, a.k.a., synchro-waveforms. The proposed methods leverage an in-depth analysis of two waveform concepts through formalized formulations: per-cycle waveform distortions and differential waveforms based on varying cycle-shift parameters. Their mathematical and empirical relationships are established, leading to algorithms that effectively identify and characterize subtle disturbances in waveform data. The methods detect and classify diverse events, including local and non-local, sub-cycle and multi-cycle, single-phase and three-phase, oscillatory and non-oscillatory, and rare as well as recurring events, and periodic disturbances. Extensive case studies, based on nearly a terabyte of real-world synchro-waveform data, provide insightful observations for each scenario.**

***Index Terms*— Synchro-waveform, event detection, feature extraction, event clustering, sub-cycle and multi-cycle events, periodic distortion, differential waveform.**

## I. Introduction

### A. Background and Motivation

Synchro-waveform is an emerging concept in grid monitoring and situational awareness. It refers to *time-synchronized* voltage and current *waveform* measurements from multiple locations in a power system; e.g., see [1]–[3].

The sensor to measure synchro-waveforms is referred to as Waveform Measurement Unit (WMU) [4]. A WMU can be compared to a Phasor Measurement Unit (PMU). However, a WMU reports time-synchronized *raw samples* of voltage and current waveforms, while a PMU uses the raw samples to calculate and report the time-synchronized *phasor representations* of the fundamental components of the measured waveforms [5]. Therefore, a WMU provides a more authentic and granular representation of voltage and current, which can reveal the most inconspicuous disturbances that are overlooked by PMUs due to their short duration or small magnitude [6].

In this paper, our focus is on the analysis of *continuous (i.e., gapless) recording* of synchro-waveform measurements, which is also referred to as time-synchronized *Continuous* Point-on-Wave (CPOW) measurements in recent literature [7], [8].

### B. Approach and Contributions

By analyzing nearly a terabyte of real-world synchro-waveform data that is continuously recorded at two sites in California and Idaho, new methods are developed and tested to detect and characterize events in synchro-waveform data. The contributions in this paper can be summarized as follows:

- A practical and theoretical foundation is developed for detecting and characterizing events in continuously recorded (gapless) synchro-waveforms. This is achieved by leveraging two key factors: changes in per-cycle waveform distortion and differential waveforms. The mathematical relationships between these factors are established, and it is demonstrated how they support the decomposition of real-world waveform measurements into steady-state and transient components. The proposed methodologies effectively identify subtle transient disturbances, providing granular insights into event dynamics that are often overlooked or difficult to capture.
- The proposed methods detect and classify a wide range of events, including local and non-local events, sub-cycle and multi-cycle events, single-phase and three-phase events, oscillatory and non-oscillatory events, rare and recurring events, as well as periodic distortions.
- A mathematical framework is introduced that links the event detection index to key characteristics of transient events, such as amplitude, damping, and the frequency of oscillatory modes. A detailed understanding of sub-cycle oscillatory events and their defining features is gained by leveraging modal analysis of differential waveforms.
- Furthermore, a method is proposed to identify and characterize recurring multi-cycle waveform events by defining waveform cycles in two different ways: using both negative-going and positive-going zero-crossings, combined with dynamic time warping. Additionally, it is investigated how analyzing differential waveforms with varying shifts in the subtracted waveform cycles can help identify periodic behavior in multi-cycle periodic events.
- This paper also presents several real-world case studies and results that can support power system operations and diagnostics. These include extracting the dominant frequency of sub-cycle oscillatory events and clustering the features of multi-cycle events with periodic distortions.

### C. Literature Review

The literature on synchro-waveforms is starting to emerge only recently. Some studies contributed to introducing this new field [1], [2]. Others explained the importance of time synchronization among waveform measurements, such as for monitoring inverter-based resources [29], [30]. There are also studies on sensor technologies [31], instrumentation [32], and

Manuscript received 6 Oct. 2024; revised 9 Feb. 2025 and 9 May 2025; accepted 10 Jun. 2025. This work is supported in part by CEC grants EPC-16-077. GridSweep devices are developed by McEachern Labs through partial funding from DOE OE and EERE. Paper no. TII-25-0855.R1. (Corresponding author: Hamed Mohsenian-Rad.)

TABLE I
OVERVIEW OF COMPARABLE LITERATURE ON EVENT DETECTION AND CHARACTERIZATION

| Reference | Data / Measurements | | | | Algorithm / Methodologies | | |
|---|---|---|---|---|---|---|---|
| | Measurement Type | Real-world Measurements[1] | Data Recording Type | Low Voltage Measurements[2] | Multi-Location Events[3] | Sub-cycle Events | Recurring Events |
| **This Paper** | Waveform | ✓ | Continuous Recording | ✓ | ✓ | ✓ | ✓ |
| [9] | Waveform | ✓ | Continuous Recording | ✓ | × | ✓ | × |
| [10] | Waveform | ✓ | Continuous Recording | × | ✓ | ✓ | × |
| [11], [12] | Waveform | ✓ | Trigger-Based Recording | × | × | ✓ | ✓ |
| [13] | Waveform | ✓ | Trigger-Based Recording | × | × | ✓ | × |
| [14], [15], [16], [17] | Waveform | ✓ | Trigger-Based Recording | × | ✓ | ✓ | × |
| [18] | Waveform | ✓ | Trigger-Based Recording | × | ✓ | × | × |
| [19] | Waveform | × | Trigger-Based Recording | - | ✓ | ✓ | × |
| [20], [21], [22], [23] | Waveform | × | Trigger-Based Recording | - | × | ✓ | × |
| [24], [25], [26], [27], [28] | Phasor | ✓ | Continuous Recording | Some | Some | × | Some |

[1] Real-world measurements refer to data collected directly from actual power systems, *not* simulations or laboratory experiments.
[2] If the voltage level of measurements is not explicitly mentioned, determination is done based on figures or overall descriptions.
[3] Multi-location events require not only access to synchronized data but also mechanisms to detect and characterize non-local events.

data compression and data storage needs [33], [34]. Various applications of synchro-waveforms have also been discussed in the literature, including fault detection [9], [16], [18], [35], fault location [15], [19], oscillation analysis [36]–[38], harmonic assessment [23], [39], wildfire mitigation [40], [41], load disaggregation [8], and frequency estimation [42].

Table I provides a comparison based on several key factors among the literature on event detection and event characterization. A critical distinction in this area is the *type* of measurements, namely waveform measurements from WMUs versus phasor measurements from phasor measurement units (PMUs). PMU data has been widely used for anomaly detection and characterization using statistical approaches [24], spectral kurtosis [25], mode decomposition [26], and machine learning [27], [28]. However, PMU data is inherently limited in capturing high-frequency and low-frequency oscillations [43] and transient dynamics [44]. Thus, this paper rather focuses on waveform measurements, which provide significantly greater visibility into voltage distortions than phasor measurements.

The next two key factors for comparison are whether the analysis is based on *real-world* measurements versus data from computer simulations or laboratory testing, and whether it uses *continuous recording* of waveform data versus *trigger-based recording*. In the latter case, waveform data are recorded only when a triggering condition is met by the sensor device, such as the built-in logic commonly used in power quality meters or fault recorders. In contrast, this paper specifically focuses on continuous recording of a large volume of real-world waveform measurements. Such measurements have only recently become available, as demonstrated in [9] and [10].

As for the work in [9] and [10], which also focus on continuous recording of real-world waveform measurements, there are several fundamental differences compared to the work in this paper. Neither [9] nor [10] develops algorithms to automatically identify recurring patterns among events, whereas this paper does so even without the use of prior labels. Here, the objective is not merely to group similar events but to determine whether the *same* event is *repeating* over time, i.e., the same phenomenon is recurring, which is critical information for uncovering minor but persistent issues such as *incipient faults*. Regarding the methodologies, the work in [9] is novel in its presentation of important observations from real-world data. However, it does not introduce new algorithms. In contrast, this paper focuses on developing algorithms and methods that are grounded in mathematical foundations and offer direct practical applications. Furthermore, with regards to the methodologies in [10], although event detection is performed in an unsupervised manner, event characterization still requires manual labeling across both time and frequency domains. In contrast, all analyses in this paper are, in essence, unsupervised, requiring no training or reliance on labels. Finally, while the methods in [10] are very novel and innovative, they are inherently more computationally intensive than the lightweight methods proposed here, due to their multi-stage design and the central role of machine learning, which inevitably adds to computational complexity.

## II. SETUP OF THE FIELD EXPERIMENTS AND EXAMPLES OF EVENTS OF INTEREST

### A. Field Experiments in California and Idaho

Two field experiments were conducted in California and Idaho using a new sensor device called GridSweep, which is plugged into 120 V power outlets [45]. GridSweeps served as WMUs to continuously record voltage waveforms. GridSweep has a sampling rate of 4.32 kHz.

Fig. 1 shows the test setup in Riverside, CA. Four GridSweep devices were used, labeled as WMU 1 to WMU 4. WMU 1 is on Phase A of a 12.47 kV feeder from Substation 1. WMUs 2, 3, and 4 are on Phases A, B, and C, respectively, in another building that is served by Substation 2. WMU 5 is a three-phase SEL 735 power quality meter at Substation 2. It has a sampling rate of 7.68 kHz. It only captures major events using an event-triggered mechanism. The experiment in California was done from October 1 to October 31.

Fig. 2 shows the test setup in Twin Falls, ID. Five GridSweep devices were used, labeled as WMU 6 to WMU 10, all on the same phase. WMU 6 and WMU 7 are on the same 12.47 kV feeder. WMU 8 and WMU 9 are on another 12.47 kV feeder, under the same substation (Substation 3). WMU 10 is on a feeder under another substation (Substation 4, three miles away from Substation 3). The experiments in Idaho took place on February 23 and 24, and on March 5, 6, and 7.

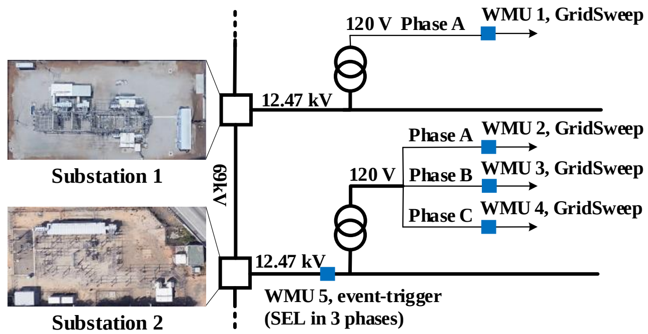


Fig. 1. Experimental setup in California, with four GridSweep WMUs to record synchro-waveforms at two buildings on two feeders, each served by a different substation. Substation 2 has a utility-grade, three-phase SEL power quality meter functioning as an event-triggered WMU.

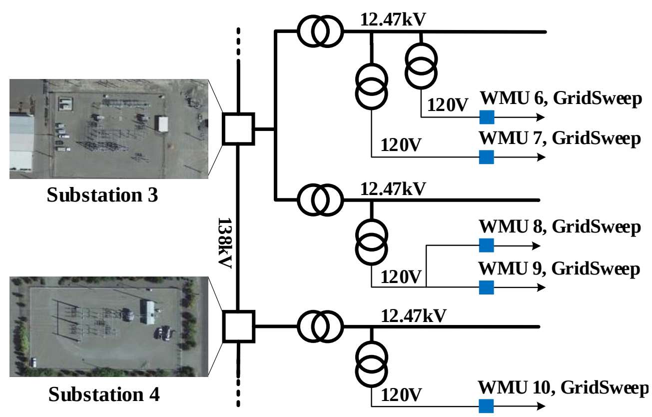


Fig. 2. Experimental setup in Idaho, with five GridSweep WMUs across four buildings on three feeders under two different substations.

All the raw measurements, together with a ReadMe documentation, are made publicly available at [46].

### B. Examples of Events of Interest

Two types of events can be distinguished in waveforms:

*1) Transient sub-cycle waveform distortions:* An example is shown in Fig. 3(a). The measurements in this example are from WMUs 2, 3, and 4. Two sub-cycle events are marked by a pair of arrows. Each event affects all three phases.

*2) Multi-cycle waveform distortions:* An example is shown in Fig. 3(b), based on the measurement from WMU 10. No waveform distortion is present in the first five cycles. In fact, there was no distortion in any cycle in the past several minutes. However, waveform distortions emerge starting from the sixth cycle. Similar distortions continue for several cycles. There are some *repetitive patterns* in the waveform distortions, which are marked by pairs of red arrows. There is also an irregularity among those patterns, marked by a single black arrow.

Next, the characterization of the events will be discussed, including both transient sub-cycle and multi-cycle events.

## III. Event Detection in Continuous Recording of Synchro-Waveforms

### A. Per-cycle Waveform Distortion Analysis

In traditional power quality analysis, it is common to calculate Total Harmonic Distortion (THD) to quantify the distortions in waveform measurements. Typically, THD is calculated over an extended period of time, such as over three seconds (180 cycles) or longer [47]. However, since the goal here is to detect and study events, a different approach is needed. In this paper, THD is rather calculated on a *per-cycle* basis.

Let $V_{\text{rms}}$ denote the RMS value of the voltage waveform measurement samples during *one* cycle. Let $V_1$ denote the magnitude of the fundamental component of the *same cycle* of the voltage waveform measurement samples, which is obtained by applying Fast Fourier Transform (FFT). The following relationship holds between $V_{\text{rms}}$, $V_1$, and THD [48, p. 142]:

$$V_{\text{rms}} = V_1\sqrt{1 + \text{THD}^2}. \tag{1}$$

After reordering the terms, we can obtain:

$$\text{THD}^2 = (V_{\text{rms}}/V_1)^2 - 1\,. \tag{2}$$

The method in (2) calculates the harmonic distortions in the waveform *without* the need to calculate *individual* harmonics. This can address two common challenges in calculating THD from individual harmonics. First, in practice, the number of harmonic orders that are included in the calculation of THD is inevitably truncated, such as up to the 50th order, resulting in approximation errors. In contrast, the method in (2) directly obtains THD by using $V_1$ and $V_{\text{rms}}$, where the latter inherently captures the contributions of all harmonic distortions without explicitly resolving each harmonic order. Second, the accuracy in calculating each individual harmonic component is often affected by factors such as noise, spectral leakage, and windowing effects, which can introduce cumulative errors when summing up all harmonic components. Therefore, using (2) is computationally more robust than calculating THD based on extracting individual harmonics.

Importantly, the value of a per-cycle $\text{THD}^2$ by itself is *not* of concern here. Our concern is rather the *changes* in the per-cycle $\text{THD}^2$. A high $\text{THD}^2$ by itself can be due to the steady-state background harmonics. In the contrary, the cycle-by-cycle changes in the $\text{THD}^2$ values can indicate the presence of an event. Let $\text{THD}^2_{\text{present}}$ denote the *present* per-cycle $\text{THD}^2$. Similarly, let $\text{THD}^2_{\text{prior}}$ denote the *prior* per-cycle $\text{THD}^2$. An event is detected when the following inequality holds:

$$\Delta\text{THD} = |\text{THD}^2_{\text{present}} - \text{THD}^2_{\text{prior}}| \geq \alpha, \tag{3}$$

where $\alpha$ is the threshold for event detection. It can serve as a control knob to adjust the level of sensitivity in event detection.

The term $\Delta$THD in (3) can be further analyzed to provide more insights about the proposed event detection method. Suppose $v_k(t)$ is the voltage waveform at cycle $k$. The length of $v_k(t)$ is one cycle. Suppose $v_{k-1}(t)$ is the voltage waveform at cycle $k-1$, also one cycle. The following relationship can be written between these two waveforms:

$$v_k(t) = v_{k-1}(t) + \Delta v_k(t), \tag{4}$$

where

$$\Delta v_k(t) = v_k(t) - v_{k-1}(t) \tag{5}$$

too has the length of one cycle, and is called the *differential waveform* at cycle $k$, as it will be discussed in more details in Section V. The expression in (4) breaks down $v_k(t)$ into two parts, a *steady-state* part which is similar to the waveform in

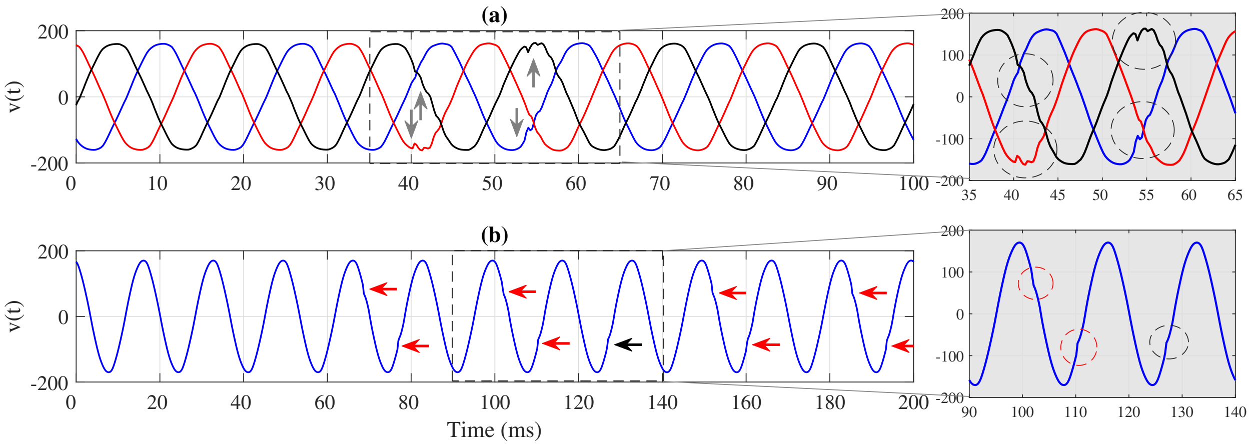

Fig. 3. Examples of events in voltage waveform: (a) three-phase measurement during two back-to-back transient sub-cycle events from the experiment in Riverside, CA; and (b) single-phase measurement during a multi-cycle event from the experiment in Twin Falls, ID. The arrows mark the distortions in the waveforms. The sole black arrow in the second sub-figure marks an irregular distortion as explained in the text.

the previous cycle, and a *transient* part which is new compared to the waveform in the previous cycle. In the absence of an event, we have $v_k(t) \approx v_{k-1}(t)$ and $\Delta v_k(t) \approx 0$. In the presence of an event, we have $v_k(t) \neq v_{k-1}(t)$ and $\Delta v_k(t) \neq 0$.

**Proposition 1**:$\Delta$THD in (3) can be approximated as follows:

$$\Delta\text{THD} \approx \frac{\text{RMS}^2\{\Delta v_k(t)\}}{\text{Fundamental}^2\{v_k(t)\}}, \tag{6}$$

where RMS$\{\cdot\}$ denotes the RMS value and Fundamental$\{\cdot\}$ denotes the magnitude of the fundamental component.

**Proof**: By substituting (2) in (3), we obtain:

$$\begin{aligned}\Delta\text{THD} = \Bigg| \left(\frac{\text{RMS}^2\{v_k(t)\}}{\text{Fundamental}^2\{v_k(t)\}} - 1\right) - \\ \left(\frac{\text{RMS}^2\{v_{k-1}(t)\}}{\text{Fundamental}^2\{v_{k-1}(t)\}} - 1\right)\Bigg| \\ = \left|\frac{\text{RMS}^2\{v_k(t)\}}{\text{Fundamental}^2\{v_k(t)\}} - \frac{\text{RMS}^2\{v_{k-1}(t)\}}{\text{Fundamental}^2\{v_{k-1}(t)\}}\right|.\end{aligned} \tag{7}$$

Next, the decomposition in (4) can be used to obtain:

$$\begin{aligned}\text{RMS}^2\{v_k(t)\} &= \text{RMS}^2\{v_{k-1}(t) + \Delta v_k(t)\} \\ &= \text{RMS}^2\{v_{k-1}(t)\} + \text{RMS}^2\{\Delta v_k(t)\} \\ &\quad + \frac{2}{T}\int_0^T v_{k-1}(t)\Delta v_k(t)dt,\end{aligned} \tag{8}$$

where $T$ is the interval of each cycle of the voltage waveform and the integral in the last term is over interval $T$. In essence, the integral calculates the *cross-correlation* between the voltage waveform in the previous cycle, i.e., $v_{k-1}(t)$ and the differential/transient voltage waveform in the current cycle, i.e., $\Delta v_k(t)$. In the absence of an event, we have $\Delta v_k(t) \approx 0$, and the integral is approximately zero. In the presence of an event, i.e., when an event initiates at cycle $k$, the differential/transient voltage waveform that is caused by the event is *unrelated* to the voltage waveform before the event; therefore, the integral is again approximately zero. It is worth adding that the sample-by-sample multiplication of the two waveforms $v_{k-1}(t)$ and $\Delta v_k(t)$ can be both positive and negative, which can cancel out each other when the integral is calculated; thus, resulting in an approximately zero cross-correlation integral. This leads to the following:

$$\text{RMS}^2\{v_k(t)\} \approx \text{RMS}^2\{v_{k-1}(t)\} + \text{RMS}^2\{\Delta v_k(t)\}. \tag{9}$$

Next, it is also noted that, in practice, the magnitude of the fundamental component of the voltage waveform does not change significantly in two consecutive cycles; therefore, the following approximation can be made:

$$\text{Fundamental}\{v_k(t)\} \approx \text{Fundamental}\{v_{k-1}(t)\}. \tag{10}$$

By substituting (9) and (10) in (7), the following is obtained:

$$\begin{aligned}\Delta\text{THD} &\approx \left|\frac{\text{RMS}^2\{v_k(t)\} - \text{RMS}^2\{v_{k-1}(t)\}}{\text{Fundamental}^2\{v_k(t)\}}\right| \\ &\approx \left|\frac{\text{RMS}^2\{\Delta v_k(t)\}}{\text{Fundamental}^2\{v_k(t)\}}\right| \\ &= \frac{\text{RMS}^2\{\Delta v_k(t)\}}{\text{Fundamental}^2\{v_k(t)\}},\end{aligned} \tag{11}$$

where the first line is due to (10), the second line is due to (9), and the third line is due to the fact that both the numerator and the denominator in the second line are always non-negative; therefore, the absolute value can be removed. ■

From (3) and the approximation in (6), an event is detected when the RMS value of the differential waveform is high compared to the magnitude of the fundamental waveform.

This interpretation of the event detection method in (3) is insightful. Despite the role that the differential waveform plays in event detection, as revealed in Proposition 1, the method in (3) does *not* require explicitly calculating the differential waveform for event detection. Nevertheless, as it will be shown in Section V, explicit calculation of the differential waveform is useful when it comes to *characterizing* a detected event.

To the best of our knowledge, the analysis in Proposition 1 marks the first instance in the literature where the RMS value of the differential waveform has been encountered.

## *B. Detecting Non-Local Events*

A *non-local* event is an event that affects voltage waveforms at *multiple* locations. To detect non-local events, the event detection outcomes across multiple WMUs at different locations

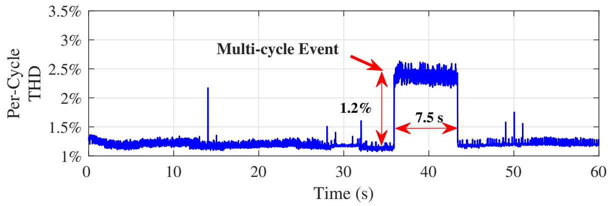


Fig. 4. Per-cycle THD profiles for one minute of voltage waveforms events during the multi-cycle event in Fig. 3(b).

must be aligned and compared. To that end, suppose $S$ WMUs are installed on a network. At each time slot, none, one, or more than one WMU may detect an event. The total number of WMUs that detect an event can be obtained as:

$$S_{\text{Event}} = \sum_{s=1}^{S} \mathbb{1}\left(\Delta\text{THD} \geq \alpha\right), \tag{12}$$

where $\mathbb{1}(\cdot)$ is the 0-1 indicator function. If $S_{\text{Event}} = 0$, then no event is detected. If $S_{\text{Event}} = 1$, then an event is detected at only one sensor location. Such event is *local*; because it did *not* cause considerable waveform distortion at other sensor locations. If $S_{\text{Event}} > 1$, an event is detected by multiple sensors. Such event is *non-local*; because it caused considerable waveform distortion at multiple sensor locations. The operator can adjust this process to require that a certain minimum number of WMUs (such as at least five WMUs) detect the event before the event is designated as non-local.

## IV. Analysis of Recurring Events

Once an event is detected, a question arises as to whether the event is an isolated occurrence or a repetition of a previously detected event. The latter would indicate the presence of a recurring phenomenon, which could provide critical insights into minor but persistent issues, such as incipient faults.

This section aims to develop a methodology to identify recurring instances of the multi-cycle event previously discussed in Fig. 3(b). The waveform distortion in this event lasted for several seconds, creating the special signature in the per-cycle THD profile that is shown in Fig. 4. Here, THD is obtained by taking the square root of the left-hand side in (2). Fig. 4 reveals several characteristics of this *multi-cycle* event. For instance, the duration of the event is 7.5 seconds, and it causes a 1.2% change in the per-cycle THD. Next, it is shown that the above event is a *recurring* event.

### A. Defining Cycles with Positive/Negative Zero-Crossing

To establish a foundation for identifying recurring events, we first examine how the definition of waveform cycles influences THD-based analysis. In fact, the signature of the intended multi-cycle event that was previously shown in the per-cycle THD profile in Fig. 4 directly depends on the definition of the cycle. Note that, the 'cycle' of a waveform can be defined from either the *negative*-going zero-crossing point, or the *positive*-going zero-crossing point. This choice can significantly alter the per-cycle THD profile, as shown in Fig. 5. If a cycle is defined based on negative-going zero-crossings, then each cycle would include one of the two back-to-back distortions at the red arrows in Fig. 3(b), resulting in the *flat shape* of the per-cycle THD signature during the event as in Fig. 5(a). However, if the cycle is defined based on positive-going zero-crossings, then one cycle would include both of the two back-to-back distortions while the next cycle would include no distortion, resulting in the *zigzag shape* of the per-cycle THD signature as in Fig. 5(b).

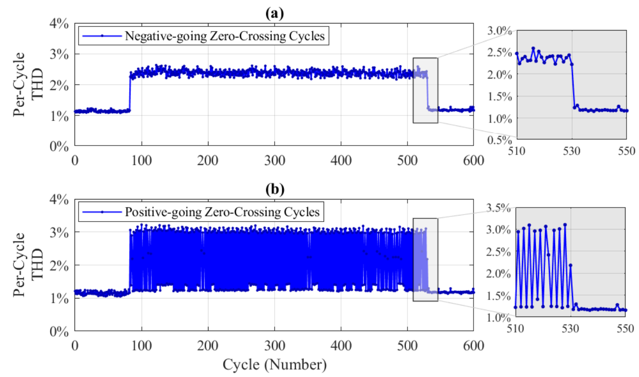


Fig. 5. The multi-cycle event in Fig. 3(b) results in two distinct signatures in per-cycle THD profile depending on how a 'cycle' is defined: (a) per-cycle THD profile using *negative*-going zero-crossings; (b) per-cycle THD profile using *positive*-going zero-crossings.

The above observation reveals how the same physical phenomenon can create different per-cycle THD profiles depending on how a cycle is defined. Hence, both choices for defining a cycle are examined to identify all instances of the event.

Accordingly, we reuse the definition of $\Delta$THD in (3) and propose to detect the *start* of a multi-cycle event by checking the following condition, which incorporates both possible definitions of cycle that we explained earlier:

$$\Delta\text{THD}_i^{(+)} \geq \alpha \quad \textbf{OR} \quad \Delta\text{THD}_i^{(-)} \geq \alpha, \tag{13}$$

where $\Delta\text{THD}_i^{(+)}$ and $\Delta\text{THD}_i^{(-)}$ are defined based on positive-going zero-crossing and negative-going zero-crossing, respectively. The start cycle of the event is denoted by $C_{\text{start}}$. Also the THD values at the start of the event are denoted by $\text{THD}_{\text{start}}^{(+)}$ and $\text{THD}_{\text{start}}^{(-)}$. Parameter $\alpha$ in (13) is a pre-determined threshold. It can be the same as the threshold in (3) in Section III-A.

Once the start of a multi-cycle event is detected, the *end* of the event is identified by checking the following condition:

$$\begin{aligned} &|\text{THD}_i^{(+)} - \text{THD}_{\text{start}}^{(+)}| \geq \beta \;\; \textbf{AND} \\ &|\text{THD}_i^{(-)} - \text{THD}_{\text{start}}^{(-)}| \geq \beta. \end{aligned} \tag{14}$$

We denote the ending cycle of the event by $C_{\text{end}}$. Parameter $\beta$ in (14) is a pre-determined threshold. We set $\alpha = 0.0002$ and $\beta = 0.006$. Higher value of $\beta$ is due to the fact that $\Delta$THD in (3) and (13) are based on the square of the THD value while the expression in (14) is based on the THD value itself.

### B. Event Signature Matching via Dynamic Time Warping

In this section, the multi-cycle event in Fig. 3(b) is used as a reference to find other similar multi-cycle events. Given $C_{\text{start}}$ and $C_{\text{end}}$, a window of per-cycle THD values is taken that starts from cycle $C_{\text{start}} - 100$ and ends at cycle $C_{\text{end}} + 100$. Here, 100 cycles before and 100 cycles after the event is included to

**Algorithm 1** Detect Recurring Multi-cycle Events

**Input:** $\Delta\text{THD}_i^{(+)}$ and $\Delta\text{THD}_i^{(-)}$ for waveform cycles.
**Output:** $C_{\text{start}}$, $C_{\text{end}}$, and Recurring Event Flag.

Set Reference Event: $\Delta\text{THD}_1^{(+)}$ and $\Delta\text{THD}_1^{(-)}$.
Set Event Flag $= 0$.
Set Recurring Event Flag $= 0$.
**for** each cycle $i$ **do**
    Obtain $\Delta\text{THD}_i^{(+)}$ and $\Delta\text{THD}_i^{(-)}$.
    **if** Event Flag $= 0$ **then**
        **if** Condition (13) Holds **then**
            % Detect Start of Event
            Record $C_{\text{start}}$, $\text{THD}_{\text{start}}^{(+)}$, and $\text{THD}_{\text{start}}^{(-)}$.
            Set Event Flag $= 1$.
        **end if**
    **else**
        **if** Condition (14) Holds **then**
            % Detect End of Event
            Record $C_{\text{end}}$.
            Obtain $\text{DTW}_{\text{PP}}$, $\text{DTW}_{\text{PN}}$, $\text{DTW}_{\text{NP}}$, $\text{DTW}_{\text{NN}}$.
            **if** Condition (21) Holds **then**
                % Detect *Recurring* Event
                Set Recurring Event Flag $= 1$.
                Exit
            **end if**
            Set Event Flag $= 0$
        **end if**
    **end if**
**end for**

make sure that the entire event signature is inside the window. Suppose the per-cycle THD values in this window are indexed from 1 to $n$, where $n = C_{\text{end}} - C_{\text{start}} + 1 + 200$. The vector of the per-cycle THD values within this window for the cycles that are defined based on the positive-going zero-crossing and the cycles that are defined based on negative-going zero-crossing, are denoted as follows:

$$\mathbf{THD}_1^{(+)} := [\text{THD}_{1,1}^{(+)}, \text{THD}_{1,2}^{(+)}, .., \text{THD}_{1,n}^{(+)}], \tag{15}$$

$$\mathbf{THD}_1^{(-)} := [\text{THD}_{1,1}^{(-)}, \text{THD}_{1,2}^{(-)}, .., \text{THD}_{1,n}^{(-)}]. \tag{16}$$

Next, suppose another multi-cycle event is detected, for which the per-cycle THD values are obtained as follows:

$$\mathbf{THD}_2^{(+)} := [\text{THD}_{2,1}^{(+)}, \text{THD}_{2,2}^{(+)}, .., \text{THD}_{2,m}^{(+)}], \tag{17}$$

$$\mathbf{THD}_2^{(-)} := [\text{THD}_{2,1}^{(-)}, \text{THD}_{2,2}^{(-)}, .., \text{THD}_{2,m}^{(-)}], \tag{18}$$

where $m$ may or may not be equal to $n$. Accordingly, we have:

$$\begin{aligned} &\text{Event 1 (Reference): } \mathbf{THD}_1^{(+)}, \mathbf{THD}_1^{(-)} \\ &\text{Event 2 (Candidate): } \mathbf{THD}_2^{(+)}, \mathbf{THD}_2^{(-)}. \end{aligned} \tag{19}$$

An event signature comparison between Event 1 and Event 2 is conducted based on the vectors in (15)-(18).

Dynamic Time Warping (DTW) [49] is proposed to compare the two time-series in (19). Since Events 1 and 2 can have different time frames, DTW is a proper metric to compare their signatures. DTW is applied to all four possible pair-wise matches of the time-series in (19) to obtain:

$$\text{DTW}_{\text{PP}} = \min_{p \in P} \; d_p(\mathbf{THD}_1^{(+)}, \mathbf{THD}_2^{(+)}), \tag{20}$$

where $d_p(\cdot, \cdot)$ is the Euclidean distance between two time-series for warping path of $p$, and $P$ is the set of all acceptable warping paths [49]. Similarly, $\text{DTW}_{\text{PN}}$ is obtained as the DTW between (15) and (18), $\text{DTW}_{\text{NP}}$ as the DTW between (16) and (17), and $\text{DTW}_{\text{NN}}$ as the DTW between (16) and (18).

Given the above DTW distances, Event 2 is considered to be a *recurrence* of Event 1 if the following condition is satisfied:

$$\min\{\text{DTW}_{\text{PP}}, \text{DTW}_{\text{PN}}, \text{DTW}_{\text{NP}}, \text{DTW}_{\text{NN}}\} \leq \gamma, \tag{21}$$

where $\gamma$ is a threshold for minimum similarity to consider Event 2 as a recurrence of Event 1. We set $\gamma = 0.001$.

The above approach is summarized in Algorithm 1.

Using Algorithm 1, 39 instances of the target event are identified across five days in Twin Falls. Table II shows the values of $\text{DTW}_{\text{PP}}$, $\text{DTW}_{\text{PN}}$, $\text{DTW}_{\text{NP}}$, and $\text{DTW}_{\text{NN}}$ for all the identified events. The minimum value according to (21), i.e., the best signature match, is highlighted in bold. Recall from Fig. 5(a) that, for the Reference Event in this example, the signature of the Reference Event is best captured when waveform cycles are defined using negative-going zero crossings. Thus, the minimum DTW values for all the candidate events in this example are achieved either in $\text{DTW}_{\text{NN}}$ or in the $\text{DTW}_{\text{NP}}$. Table III shows the start and end time of all the identified recurring events. Seven instances occurred on Test Day 1, and eight instances occurred on Test Days 2 through 5. There are similarities in the timing of these 39 events.

### *C. Clustering of the Multi-Cycle Periodic Events*

To further analyze the 39 detected multi-cycle periodic events in Table III, the following four features are considered that represent different characteristics of these events:

- **Event Duration**: The number of cycles during the event. For example, the first event (Reference Event) lasted 448 cycles (about 7.5 seconds) as it is marked with the *horizontal* double-arrow in Fig. 4.
- **Change in Per-Cycle THD Level**: This is obtained based on the per-cycle THD at the start of the event. For the Reference Event, the change in the per-cycle THD is 1.2%, marked with a *vertical* double-arrow in Fig. 4.
- **Time of Day**: The time when the event occurred, expressed in hour. For example, for the Reference Event, this feature is obtained as $2 + 36/60 + 5/3600 = 2.60139$.
- **Number of Irregular Cycles**: As it was discussed in Section II-B, apart from the repeated distortions that are marked with the pairs of red arrows in Fig. 3(b), the waveforms in this event also have some occasional irregular distortions, such as the one that is marked with the black arrow. The number of cycles with irregular distortions is used as another feature. For instance, the Reference Event has 20 cycles with irregular distortions.

The above features are shown in Fig. 6. Three features demonstrate clear distinctions between two variations of the recurring multi-cycle events in Table III. While 29 out of 39 events lasted 448 cycles, including the Reference Event, the remaining 10 events lasted 416 cycles; see Fig. 6(a). All the 10 events with shorter duration occurred between 6 to 8 AM, while the longer events took place in other times; see Fig. 6(c).

TABLE II
ANALYSIS OF SIGNATURE MATCHING USING VARIOUS PAIRWISE DTW COMBINATIONS FOR ALL RECURRING EVENTS COMPARED TO THE REFERENCE EVENT (EVENT 1)

| Event No. | $DTW_{PP}$ | $DTW_{PN}$ | $DTW_{NP}$ | $DTW_{NN}$ |
|---|---|---|---|---|
| 1 | Reference Event | | | |
| 2 | 0.0018 | 0.0317 | 0.0335 | **0.0001** |
| 3 | 0.0327 | 0.0046 | **0.0002** | 0.0333 |
| 4 | 0.0040 | 0.0330 | 0.0335 | **0.0002** |
| 5 | 0.0317 | 0.0019 | **0.0002** | 0.0388 |
| 6 | 0.0022 | 0.0323 | 0.0375 | **0.0002** |
| 7 | 0.0018 | 0.0315 | 0.0314 | **0.0001** |
| 8 | 0.0021 | 0.0322 | 0.0349 | **0.0002** |
| 9 | 0.0022 | 0.0309 | 0.0379 | **0.0003** |
| 10 | 0.0042 | 0.0329 | 0.0304 | **0.0002** |
| 11 | 0.0317 | 0.0038 | **0.0002** | 0.0333 |
| 12 | 0.0324 | 0.0019 | **0.0002** | 0.0374 |
| 13 | 0.0313 | 0.0041 | **0.0010** | 0.0436 |
| 14 | 0.0320 | 0.0017 | **0.0002** | 0.0316 |
| 15 | 0.0019 | 0.0323 | 0.0320 | **0.0002** |
| 16 | 0.0330 | 0.0023 | **0.0003** | 0.0342 |
| 17 | 0.0333 | 0.0021 | **0.0002** | 0.0357 |
| 18 | 0.0327 | 0.0051 | **0.0002** | 0.0327 |
| 19 | 0.0044 | 0.0342 | 0.0343 | **0.0004** |
| 20 | 0.0023 | 0.0342 | 0.0354 | **0.0005** |
| 21 | 0.0345 | 0.0023 | **0.0004** | 0.0342 |
| 22 | 0.0019 | 0.0331 | 0.0312 | **0.0003** |
| 23 | 0.0333 | 0.0018 | **0.0003** | 0.0308 |
| 24 | 0.0020 | 0.0333 | 0.0354 | **0.0002** |
| 25 | 0.0340 | 0.0021 | **0.0005** | 0.0336 |
| 26 | 0.0340 | 0.0054 | **0.0004** | 0.0308 |
| 27 | 0.0335 | 0.0039 | **0.0002** | 0.0330 |
| 28 | 0.0322 | 0.0019 | **0.0002** | 0.0376 |
| 29 | 0.0315 | 0.0023 | **0.0003** | 0.0393 |
| 30 | 0.0018 | 0.0323 | 0.0337 | **0.0001** |
| 31 | 0.0022 | 0.0341 | 0.0328 | **0.0004** |
| 32 | 0.0325 | 0.0006 | **0.0002** | 0.0376 |
| 33 | 0.0337 | 0.0020 | **0.0004** | 0.0365 |
| 34 | 0.0333 | 0.0048 | **0.0008** | 0.0334 |
| 35 | 0.0041 | 0.0338 | 0.0323 | **0.0003** |
| 36 | 0.0008 | 0.0331 | 0.0368 | **0.0003** |
| 37 | 0.0319 | 0.0024 | **0.0004** | 0.0374 |
| 38 | 0.0312 | 0.0011 | **0.0003** | 0.0375 |
| 39 | 0.0329 | 0.0017 | **0.0001** | 0.0338 |

TABLE III
TIMING OF RECURRING MULTI-CYCLE PERIODIC EVENTS

| Event No. | Starting Time | End Time | Event No. | Starting Time | End Time |
|---|---|---|---|---|---|
| | Test Day 1 | | | Test Day 3 (Cont.) | |
| 1 | 02:36:05 | 02:36:13 | 21 | 12:38:01 | 12:38:08 |
| 2 | 04:37:49 | 04:37:57 | 22 | 18:36:09 | 18:36:17 |
| 3 | 07:24:29 | 07:24:36 | 23 | 20:37:11 | 20:37:19 |
| 4 | 08:39:01 | 08:39:08 | | Test Day 4 | |
| 5 | 10:58:22 | 10:58:29 | 24 | 02:36:06 | 02:36:14 |
| 6 | 12:39:38 | 12:39:46 | 25 | 04:38:54 | 04:39:01 |
| 7 | 21:07:34 | 21:07:42 | 26 | 07:19:42 | 07:19:49 |
| | Test Day 2 | | 27 | 08:45:43 | 08:45:50 |
| 8 | 02:36:03 | 02:36:10 | 28 | 12:13:39 | 12:13:47 |
| 9 | 04:37:39 | 04:37:47 | 29 | 13:51:13 | 13:51:20 |
| 10 | 08:26:44 | 08:26:51 | 30 | 18:36:01 | 18:36:09 |
| 11 | 09:34:47 | 09:34:54 | 31 | 20:48:48 | 20:48:56 |
| 12 | 11:24:17 | 11:24:25 | | Test Day 5 | |
| 13 | 12:59:50 | 12:59:57 | 32 | 02:35:45 | 02:35:53 |
| 14 | 18:36:05 | 18:36:12 | 33 | 04:48:57 | 04:49:04 |
| 15 | 20:54:45 | 20:54:52 | 34 | 07:20:52 | 07:20:59 |
| | Test Day 3 | | 35 | 08:35:45 | 08:35:53 |
| 16 | 02:50:45 | 02:50:53 | 36 | 10:54:56 | 10:55:04 |
| 17 | 04:38:01 | 04:38:08 | 37 | 12:39:33 | 12:39:41 |
| 18 | 07:21:21 | 07:21:28 | 38 | 18:45:05 | 18:45:12 |
| 19 | 08:35:51 | 08:35:58 | 39 | 20:35:46 | 20:35:54 |
| 20 | 10:52:35 | 10:52:42 | | | |

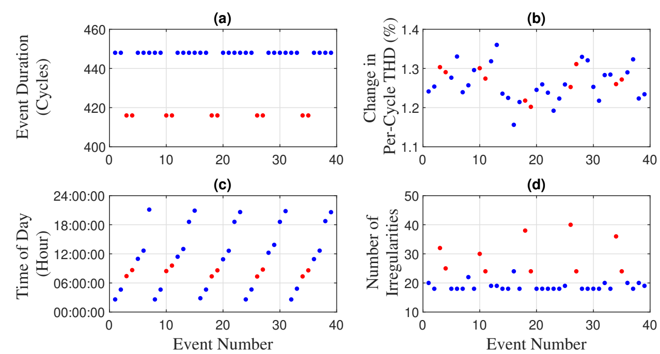


Fig. 6. The four features introduced in Section IV-C, for all 39 recurring events in Table III. These recurring events can be divided into *two clusters* as marked by two different colors, blue and red. The two clusters are clearly *separable* based on the scatter plots in (a), (c), and (d). The Reference Event (Event 1) belongs to the blue cluster.

The longer events almost always had either 19 or 20 irregular cycles, while the shorter events had up to 40 irregular cycles; see Fig. 6(d). The feature on the change in per-cycle THD does *not* seem to indicate a clear distinction between the two variations of these recurring multi-cycle events.

By applying $k$-means clustering [50] to the above features, the recurring multi-cycle events in Table III are divided into two *clusters*, marked in blue and red in Fig. 6.

The combination of the analysis in Sections IV-A, IV-B, and IV-C provides a powerful toolbox to detect, identify, and characterize the recurring instances of an event of interest.

## V. DIFFERENTIAL WAVEFORM ANALYSIS FOR FURTHER EVENT CHARACTERIZATION

Recall from Proposition 1 that the concept of differential waveform plays an *implicit* role in the process of detecting an event. In this section, the differential waveform is explicitly extracted for the purpose of characterizing different types of detected events. Furthermore, the initial definition of differential waveform in (5) is broadened.

Let $v(t)$ denote the raw voltage waveform during an event. The differential waveform can be more broadly defined as:

$$\Delta v(t) = v(t) - v(t - NT), \tag{22}$$

where $N$ is a small integer, such as 1, 2, 3, 4, or 5; see [48, p. 151]. If $N = 1$, then the expression in (22) reduces to the one in (5). Here, $v(t - NT)$ serves as a *reference* for the "normal" waveform behavior *before* the event happens. The subtraction in (22) can approximately remove the normal portion of the waveform, leaving only the *event signature* that is superposed to the normal waveform. The differential waveform in (22) is also sometimes referred to as *cycle-delayed* waveform [51].

### *A. Analysis of Sub-cycle Oscillatory Events*

Oscillatory events can be studied by examining the *modal analysis* of the differential waveforms. The differential waveform at cycle $k$, as previously defined in (5), is considered.

Using modal analysis, $\Delta v_k(t)$ can be expressed as follows:

$$\Delta v_k(t) = \sum_{m=1}^{M} B_{k,m}\exp(-\sigma_{k,m}t)\cos\left(2\pi f_{k,m}t + \psi_{k,m}\right), \tag{23}$$

where $M$ is the number of *oscillatory modes*. For each mode $m$, notations $B_{k,m}$, $\psi_{k,m}$, $f_{k,m}$, and $\sigma_{k,m} > 0$ indicate the amplitude, phase angle, frequency, and damping factor.

**Proposition 2**: From the modal in (23), the following can be derived for a sub-cycle waveform oscillatory event:

$$\mathrm{RMS}^2\{\Delta v_k(t)\} \approx \frac{1}{4T}\sum_{m=1}^{M}\frac{B_{k,m}^2}{\sigma_{k,m}}\left(1 - \exp(-2\sigma_{k,m}T)\right). \tag{24}$$

If the sub-cycle oscillation has a *dominant* mode ($B_k$, $\psi_k$, $f_k$, $\sigma_k$), then the expression in (24) can be simplified as follows:

$$\mathrm{RMS}^2\{\Delta v_k(t)\} \approx \frac{1}{4T}\frac{B_k^2}{\sigma_k}\left(1 - \exp(-2\sigma_k T)\right). \tag{25}$$

The above expression is *monotone increasing* in $B_k$ and *monotone decreasing* in $\sigma_m > 0$. From (6) and (25), $\Delta$THD is *directly* related to the amplitude and *inversely* related to the damping factor of the dominant sub-cycle oscillatory mode.

**Proof**: By taking the RMS value of (23), and using trigonometric identity $\cos^2(\theta) = (1 + \cos(2\theta))/2$, we obtain:

$$\begin{aligned}\mathrm{RMS}^2\{\Delta v_k(t)\} = \frac{1}{T}\int_0^T \sum_{m=1}^{M}\frac{B_{k,m}^2}{2}\exp(-2\sigma_{k,m}t)\,dt\ + \\ \frac{1}{T}\int_0^T \sum_{m=1}^{M}\frac{B_{k,m}^2}{2}\exp(-2\sigma_{k,m}t)\cos\left(2(2\pi f_{k,m}t + \psi_{k,m})\right)dt + \\ \frac{1}{T}\int_0^T \sum_{m=1}^{M}\sum_{\substack{n=1\\ n\neq m}}^{M} B_{k,m}B_{k,n}\exp(-(\sigma_{k,m} + \sigma_{k,n})t)\ \times \\ \cos(2\pi f_{k,m}t + \psi_{k,m})\cos(2\pi f_{k,n}t + \psi_{k,n})\,dt.\end{aligned} \tag{26}$$

The integral in the first line of (26) is equal to the right-hand side of (24). Given the *sub-cycle* nature of the damping oscillations, we can assume that $f_{k,m} \gg 1/T$, i.e., the frequencies of the damping *sub-cycle* oscillations are much higher than the fundamental frequency $1/T$. Thus, the integral on the second line of (26), which is over interval $T$, is approximately zero. As for the integral on the third line of (26), it is over *orthogonal* frequencies. Hence, this integral is also zero. Thus, (24) can be concluded; which also leads to (25). ■

From (6) in Proposition 1 and (25) in Proposition 2, a sub-cycle oscillatory event is more likely to be detected if it has a *larger* amplitude and a *smaller* damping factor.

As an example, consider the raw waveform measurements in Fig. 7(a) that are recorded by WMU 2 (Phase A), WMU 3 (Phase B), and WMU 4 (Phase C) during a three-phase sub-cycle event. Fig. 7(b) shows the differential waveform on each phase, where the event signature is more distinctly visible.

During the one-month experiment in Riverside, a total of 26 sub-cycle oscillatory events were observed. All of them, including the one in Fig. 7, were non-local events that were observed by all WMUs under both Substations 1 and 2.

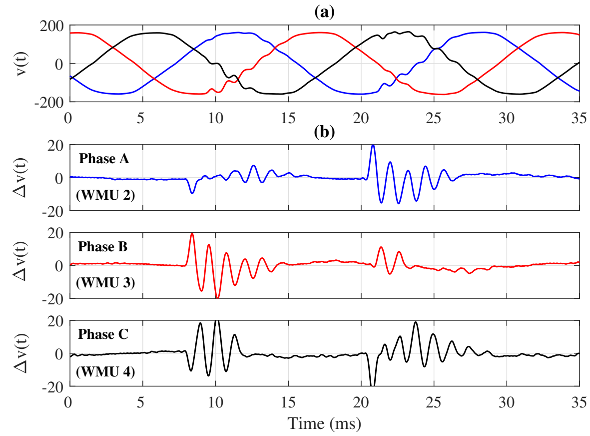


Fig. 7. Extracting the differential waveforms during a three-phase sub-cycle oscillation event: (a) raw waveforms in which the event's signatures are dominated by the steady-state waveforms; (b) differential waveforms for each phase, in which the effect of the event can be clearly seen.

Fig. 8(a) illustrates the values of $\Delta$THD at WMU 1 versus the corresponding values of $\Delta$THD at WMU 2 for all the 26 sub-cycle oscillatory events. For almost all these events, $\Delta$THD is larger at WMU 2 than at WMU 1, suggesting that these events create stronger distortions in the voltage waveforms at WMU 2. From Proposition 1, $\Delta$THD can be approximately obtained based on the fraction in (6). This is illustrated in Fig. 8(b). Notice that the same overall observation from Fig. 8(a) is evident also in this figure. Finally, from Proposition 1 together with Proposition 2, the strength of $\Delta$THD at each WMU is *inversely* related to the damping factor $\sigma$ for the dominant mode of oscillation, see (25). Such inverse relationship is clearly visible in the scatter plot in Fig. 8(c). Compared to the points in Figs. 8(a) and 8(b), the points in Fig. 8(c) have significantly moved *down* and to the *right*; thus confirming the analytical perspective in Propositions 1 and 2.

The results in Fig. 8(c) are based on Prony analysis [48, pp. 58-61], which is a method to extract the model representation in (23). However, FFT can also be used to extract the *dominant frequency* of oscillations in sub-cycle oscillatory events.

Applying FFT to the differential waveforms in Fig. 7(b) reveals the dominant frequency of the oscillations as 842 Hz on all phases. This event was captured also by WMU 5 at Substation 2. At WMU 5, the dominant frequency is 834 Hz on all phases, which is close to the oscillation frequency at 842 Hz that was obtained by WMUs 2, 3, and 4. The slight discrepancy is due to the higher sampling rate of WMU 5, as it was previously explained in Section II-A.

Fig. 9 shows the dominant frequency of all the 26 oscillatory events by applying FFT to the differential waveforms of each event, at WMU 1, under Substation 1, versus WMU 2, under Substation 2. Most events displayed similar frequencies at WMU 1 and WMU 2, marked as "diagonal". Only four events showed different dominant frequencies, marked as "off-diagonal". It is possible that the dynamics of the system and the circuit result in different frequencies at different locations.

## *B. Analysis of Local and Non-Local Oscillatory Events*

The differential waveforms from *several* WMUs can offer in-depth insights into local and non-local events. Next, two

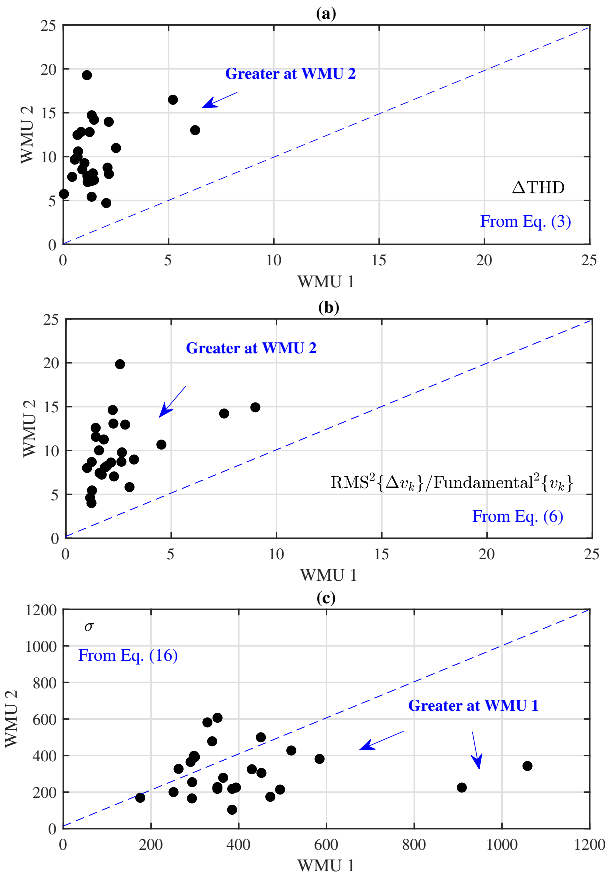


Fig. 8. The characteristics of the sub-cycle oscillatory events across WMU 1 and WMU 2 with respect to the results in Propositions 1 and 2: (a) $\Delta$THD in percentage where points above the diagonal indicate a greater $\Delta$THD at WMU 2; (b) the fraction in (6) in percentage, showing the direct relationship with such fraction and $\Delta$THD; thus confirming Proposition 1; and (c) the damping ratio $\sigma$, showing the inverse relationship in (25); thus confirming Proposition 2.

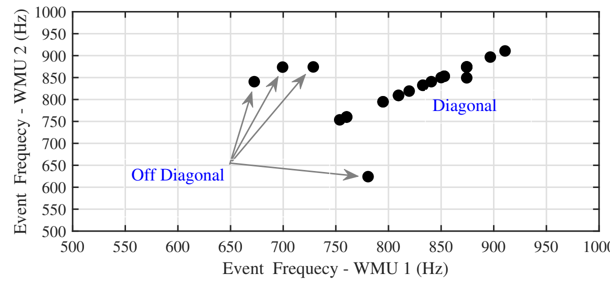


Fig. 9. Oscillation frequency for each non-local oscillatory event based on frequency calculations at two locations of WMU 1 and WMU 2.

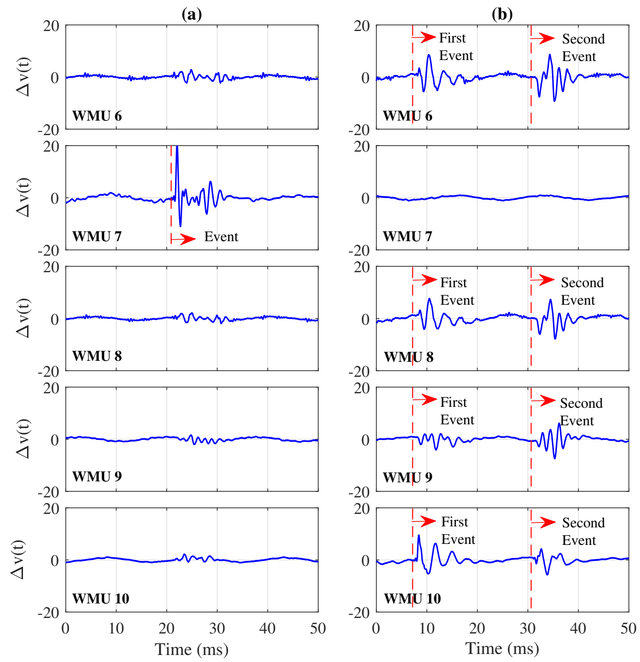


Fig. 10. Differential waveforms for local and non-local events: (a) a local event at WMU 7, with no signature at other locations; (b) a two-part non-local event recorded by WMUs 6, 8, 9, 10, but absent at WMU 7.

example events are presented from Twin Falls to demonstrate the varying impact of the events across different locations.

First, consider the time-synchronized differential waveforms in Fig. 10(a). An oscillatory event is visible only at WMU 7, with minor signatures at WMUs 6, 8, 9, and 10. This event is a *local* event. Next, consider the time-synchronized differential waveforms in Fig. 10(b), which shows another oscillatory event, where the event signature is visible at four (of the five) WMUs in this experiment. Therefore, this is a *non-local* event.

Fig. 11 shows the spectral analysis of the time-synchronized differential waveforms (based on applying FFT) during the event that was previously shown in Fig. 10(b). All four WMUs observed the same *dominant frequency* of 323 Hz at their locations; see the blue bin in Figs. 11(a), (b), (c), and (d).

### *C. Analysis of Multi-Cycle Periodic Events*

Differential waveforms can also help detect and characterize *periodic* events. The key here is to obtain the differential waveforms for different values of $N$ and compare the results. This is because periodic distortions can *cancel out* each other.

For instance, for the event in Fig. 3(b), the differential waveform is shown in Fig. 12(a) for $N = 1$, and in Fig. 12(b) for $N = 2$. The event signatures are visible in Fig. 12(a) in the form of several spikes. There are far fewer spikes in Fig. 12(b), 6 versus 13; because they *cancel out* each other when $N = 2$. This is because the periodic distortions in Fig. 3(b) have a period of two cycles, except for the irregularity that was marked with the black arrow in Fig. 3(b). Four spikes are marked in Fig. 12(b) are labeled "Due to Irregular Distortion". They are all due to the presence of the irregularly distorted cycle during the event, as they disrupt the periodic patterns.

Next, the above observation is turned into an algorithm. For each value of $N$, the average RMS value of $\Delta v(t)$ during all the cycles of the multi-cycle event is calculated. The results for different values of $N$ are placed into a single vector $\overline{\text{RMS}}_{\Delta v}$. For instance, for the raw waveform in Fig. 3(b), the differential waveforms for $N = 1, 2, 3, 4, 5,$ and 6 are examined to obtain:

$$\overline{\text{RMS}}_{\Delta v} = [\ 2.87 \quad 1.00 \quad 2.75 \quad 1.36 \quad 2.70 \quad 1.35\ ]. \tag{27}$$

Notice that in (27), the average RMS value of $\Delta v(t)$ is twice larger for $N = 1, 3,$ and 5, than for $N = 2, 4,$ and 6. The following *sign* vector is then defined accordingly:

$$\text{SGN}_{\Delta v} = sign\left(\overline{\text{RMS}}_{\Delta v} - mean\left(\overline{\text{RMS}}_{\Delta v}\right)\right). \tag{28}$$

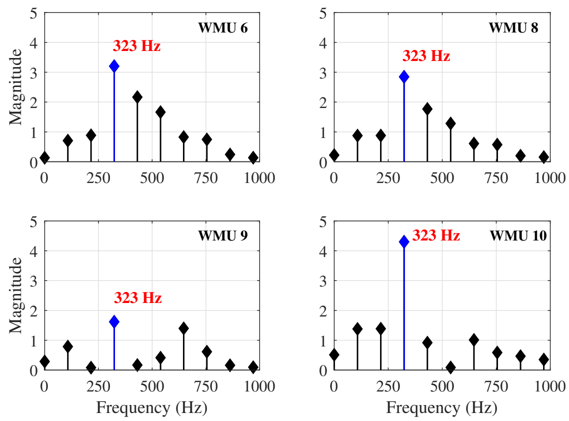


Fig. 11. FFT analysis of the differential waveform for the same non-local event, at four locations where it was observed, indicates that the dominant oscillation frequency is consistent across all four locations.

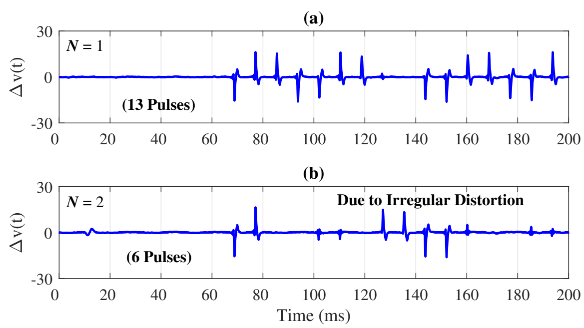


Fig. 12. Differential waveform for the first few cycles of the multi-cycle event from Fig. 3(b), using $N = 1$ cycle; (b) $N = 2$ cycles.

For example, the sign vector for the RMS values in (27) is

$$\mathrm{SGN}_{\Delta v} = [\,+1\ -1\ +1\ -1\ +1\ -1\,]. \tag{29}$$

The fact that the raw waveform in Fig. 3(b) has a period of *two* is clearly visible in (29). As another example, if the periodic waveform distortions occur once every *three* cycles, then the average RMS values of the differential waveforms can be examined for $N = 1, 2, 3, 4, 5,$ and 6 to obtain:

$$\mathrm{SGN}_{\Delta v} = [\,+1\ +1\ -1\ +1\ +1\ -1\,]. \tag{30}$$

Again, the fact that the raw waveform has a period of *three* is clearly visible in the sign vector in (30). The period of the periodic waveform distortions can be obtained by obtaining the period of the sign vector in (28). This can be done by a simple *auto-correlation* analysis to the sign vector, as follows:

$$\mathrm{AC}_{\Delta v} = \text{Auto-Correlation}\{\mathrm{SGN}_{\Delta v}\}, \tag{31}$$

where auto-correlation is calculated such as by using *autocorr* in MATLAB [52]. The auto-correlation vector in (31) measures the similarity between the *original* vector $\mathrm{SGN}_{\Delta v}$ and a *shifted* version of vector $\mathrm{SGN}_{\Delta v}$, where the shifting is from $k = 0$ (no shift) to $k = \mathrm{Length}\{\mathrm{SGN}_{\Delta v}\} - 1$. Accordingly, vector $\mathrm{AC}_{\Delta v}$ has the same length as vector $\mathrm{SGN}_{\Delta v}$. Period $P$ of a multi-cycle periodic event is identified as the *non-zero* shift, i.e., $k > 0$, at which the value of $\mathrm{AC}_{\Delta v}$ is maximum:

$$P = \arg\max_{k>0}\ \mathrm{AC}_{\Delta v}[k]. \tag{32}$$

The above process is summarized in Algorithm 2.

**Algorithm 2** Detect Periodic Multi-cycle Events

**Input:** Raw waveform $v(t)$, Maximum cycle delay $N^{\max}$.
**Output:** Detected period $P$.
Suppose Condition (3) Holds $\rightarrow$ An Event is Detected.
Set $\overline{\mathrm{RMS}}_{\Delta v} = [\,]$.
**for** $N = 1$ to $N^{\max}$ **do**
  Obtain $\Delta v(t)$ as in (22) for the Given $N$.
  Obtain RMS Value of $\Delta v(t)$.
  Append $\overline{\mathrm{RMS}}_{\Delta v}$ by the RMS Value of $\Delta v(t)$.
**end for**
Obtain $\mathrm{SGN}_{\Delta v}$ in (28).
Obtain $\mathrm{AC}_{\Delta v}$ in (31)
Calculate $P$ as in (32)

TABLE IV
ANALYSIS OF MULTI-CYCLE PERIODIC EVENTS FOR DETECTING THEIR PERIODICITY

| Event No. | $\overline{\mathrm{RMS}}_{\Delta v}$ | $\mathrm{SGN}_{\Delta v}$ | $P$ |
|---|---|---|---|
| 1 | [ 2.89 1.00 2.78 1.38 2.73 1.36 ] | [ +1 −1 +1 −1 +1 −1 ] | 2 |
| 2 | [ 2.91 1.05 2.85 1.54 2.89 1.68 ] | [ +1 −1 +1 −1 +1 −1 ] | 2 |
| 3 | [ 2.78 1.34 2.63 1.87 2.60 2.00 ] | [ +1 −1 +1 −1 +1 −1 ] | 2 |
| 4 | [ 2.81 1.24 2.72 1.73 2.73 1.81 ] | [ +1 −1 +1 −1 +1 −1 ] | 2 |
| 5 | [ 2.94 1.22 2.99 1.88 3.18 2.33 ] | [ +1 −1 +1 −1 +1 −1 ] | 2 |
| 6 | [ 2.90 0.98 2.79 1.34 2.74 1.25 ] | [ +1 −1 +1 −1 +1 −1 ] | 2 |
| 7 | [ 2.93 1.13 2.88 1.57 2.91 1.64 ] | [ +1 −1 +1 −1 +1 −1 ] | 2 |
| 8 | [ 2.92 1.33 2.97 2.08 3.23 2.57 ] | [ +1 −1 +1 −1 +1 +1 ] | 2 |
| 9 | [ 2.93 1.23 3.02 2.06 3.36 2.68 ] | [ +1 −1 +1 −1 +1 +1 ] | 2 |
| 10 | [ 2.76 1.18 2.57 1.63 2.45 1.70 ] | [ +1 −1 +1 −1 +1 −1 ] | 2 |
| 11 | [ 2.80 1.21 2.71 1.71 2.72 1.78 ] | [ +1 −1 +1 −1 +1 −1 ] | 2 |
| 12 | [ 2.94 1.28 3.03 2.03 3.29 2.57 ] | [ +1 −1 +1 −1 +1 +1 ] | 2 |
| 13 | [ 2.93 1.11 2.87 1.54 2.87 1.56 ] | [ +1 −1 +1 −1 +1 −1 ] | 2 |
| 14 | [ 2.94 1.13 2.92 1.70 3.03 2.02 ] | [ +1 −1 +1 −1 +1 −1 ] | 2 |
| 15 | [ 2.94 1.17 2.95 1.80 3.14 2.19 ] | [ +1 −1 +1 −1 +1 −1 ] | 2 |
| 16 | [ 2.89 1.15 2.81 1.72 2.89 1.94 ] | [ +1 −1 +1 −1 +1 −1 ] | 2 |
| 17 | [ 2.94 1.21 2.99 1.95 3.26 2.48 ] | [ +1 −1 +1 −1 +1 +1 ] | 2 |
| 18 | [ 2.75 1.42 2.58 2.07 2.64 2.32 ] | [ +1 −1 +1 −1 +1 +1 ] | 2 |
| 19 | [ 2.79 1.26 2.77 1.93 2.97 2.33 ] | [ +1 −1 +1 −1 +1 −1 ] | 2 |
| 20 | [ 2.91 1.02 2.81 1.42 2.77 1.43 ] | [ +1 −1 +1 −1 +1 −1 ] | 2 |
| 21 | [ 2.93 1.20 2.94 1.81 3.10 2.13 ] | [ +1 −1 +1 −1 +1 −1 ] | 2 |
| 22 | [ 2.92 1.11 2.90 1.67 3.10 1.99 ] | [ +1 −1 +1 −1 +1 −1 ] | 2 |
| 23 | [ 2.95 1.17 2.94 1.74 3.05 1.99 ] | [ +1 −1 +1 −1 +1 −1 ] | 2 |
| 24 | [ 2.93 1.19 2.93 1.78 3.06 2.10 ] | [ +1 −1 +1 −1 +1 −1 ] | 2 |
| 25 | [ 2.95 1.31 3.03 2.02 3.30 2.52 ] | [ +1 −1 +1 −1 +1 −1 ] | 2 |
| 26 | [ 2.76 1.55 2.65 2.29 2.81 2.61 ] | [ +1 −1 +1 −1 +1 +1 ] | 2 |
| 27 | [ 2.78 1.14 2.67 1.67 2.70 1.80 ] | [ +1 −1 +1 −1 +1 −1 ] | 2 |
| 28 | [ 2.92 1.13 2.92 1.78 3.08 2.18 ] | [ +1 −1 +1 −1 +1 −1 ] | 2 |
| 29 | [ 2.91 1.12 2.92 1.78 3.10 2.17 ] | [ +1 −1 +1 −1 +1 −1 ] | 2 |
| 30 | [ 2.92 1.02 2.83 1.42 2.80 1.46 ] | [ +1 −1 +1 −1 +1 −1 ] | 2 |
| 31 | [ 2.92 1.03 2.83 1.44 2.82 1.43 ] | [ +1 −1 +1 −1 +1 −1 ] | 2 |
| 32 | [ 2.89 1.00 2.77 1.37 2.72 1.33 ] | [ +1 −1 +1 −1 +1 −1 ] | 2 |
| 33 | [ 2.92 1.11 2.86 1.54 2.87 1.58 ] | [ +1 −1 +1 −1 +1 −1 ] | 2 |
| 34 | [ 2.77 1.47 2.69 2.17 2.83 2.52 ] | [ +1 −1 +1 −1 +1 +1 ] | 2 |
| 35 | [ 2.78 1.19 2.69 1.72 2.76 1.91 ] | [ +1 −1 +1 −1 +1 −1 ] | 2 |
| 36 | [ 2.90 1.03 2.79 1.42 2.76 1.44 ] | [ +1 −1 +1 −1 +1 −1 ] | 2 |
| 37 | [ 2.92 1.21 2.97 1.91 3.23 2.40 ] | [ +1 −1 +1 −1 +1 −1 ] | 2 |
| 38 | [ 2.93 1.03 2.82 1.41 2.77 1.41 ] | [ +1 −1 +1 −1 +1 −1 ] | 2 |
| 39 | [ 2.94 1.13 2.88 1.55 2.89 1.58 ] | [ +1 −1 +1 −1 +1 −1 ] | 2 |

### D. Period Calculation of the Multi-Cycle Periodic Events

Recall from Section IV-B that a total of 39 recurring events were identified and listed in Table III. All those events are periodic. In this section, we apply Algorithm 2 to all the 39 events that we previously listed in Table III to obtain the period of their waveform distortions. The results are shown in Table IV. In each row, i.e., for each event, the table provides vectors $\overline{\mathrm{RMS}}_{\Delta v}$ and $\mathrm{SGN}_{\Delta v}$, where parameter $N^{\max} = 6$, as well as the distortion period estimation result $P$. Notice that the period of distortions is obtained at $P = 2$ for *all* the 39 recurring events. This clearly shows the consistency in the results, as well as the fact that these events are indeed recurring events.

Next, we note that there are two outcomes for $\mathrm{SGN}_{\Delta v}$ in Table IV, either $\mathrm{SGN}_{\Delta v} = [+1 \quad -1 \quad +1 \quad -1 \quad +1 \quad -1]$

or $\mathrm{SGN}_{\Delta v} = [+1 \quad -1 \quad +1 \quad -1 \quad +1 \quad +1]$. The former occurs much more frequently, but the latter also occurs in a few events. The auto-correlation vectors corresponding to these two cases of $\mathrm{SGN}_{\Delta v}$ are $\mathrm{AC}_{\Delta v} = [+1.00 \;\vdots\; -0.83 \;\; \mathbf{+0.67} \;\; -0.50 \;\; +0.33 \;\; -0.17]$ and $\mathrm{AC}_{\Delta v} = [+1.00 \;\vdots\; -0.50 \;\; \mathbf{+0.33} \;\; -0.17 \;\; 0.00 \;\; +0.17]$, respectively. Therefore, despite the differences between the two instances of $\mathrm{SGN}_{\Delta v}$, the two auto-correlation vectors have their maximum values at the same entry. Hence, the exact same period is obtained by Algorithm 2 in both cases, with $P = 2$.

If parameter $N^{\max}$ is increased, then more variations of vector $\mathrm{SGN}_{\Delta v}$ may occur among the recurring events. This is illustrated in Table V. Here, parameter $N^{\max}$ is increased from 6 to 7, 8, 9, and 10. Note that, the number of $\mathrm{SGN}_{\Delta v}$ variations among the recurring events increases to 2, 3, 5, and 6, respectively. Nevertheless, the auto-correlation results consistently yield the same value for $P$. In other words, although increasing $N^{\max}$ leads to more diverse instances of $\mathrm{SGN}_{\Delta v}$, the auto-correlation results continue to provide the exact same estimation for the period of the periodic waveform distortions, namely $P = 2$. Interestingly, the same final results are obtained even if parameter $N^{\max}$ is decreased from 6 to 5, as we can see in the first row in Table V. The results in Table V clearly demonstrate the robustness of the proposed method in estimating the period of the periodic waveform distortions.

## VI. Conclusions and Future Work

This paper offers an extensive analysis of event detection and event characterization in real-world continuous recording of synchro-waveforms in power systems. The methods are built upon mathematical analysis of key waveform features and characteristics. Different types of events were analyzed, including local and non-local events, sub-cycle and multi-cycle events, single-phase and three-phase events, and oscillatory and non-oscillatory events. Various features were extracted and analyzed, derived from the raw waveform measurements, the differential waveforms, and the event signatures in the per-cycle waveform distortion profiles. New algorithms were proposed to address the subtle challenges in handling synchro-waveform data in practice, such as the impact of defining cycles based on negative-going versus positive-going zero-crossing, as well as the impact of delay parameter in the analysis of differential waveforms. Several case studies were presented to systematically summarize the results for different types of events, with focus on oscillatory events, recurring disturbances, and periodic distortions.

The methods in this paper can be used in various smart grid applications, such as asset monitoring to detect and characterize malfunctions in capacitors, transformers, underground and overhead power lines, and inverter-based resources. Due to the low cost of sensor installation at power outlets, the analysis of event signatures in synchro-waveforms from grid-edge sensor technologies can be a promising low-cost option to enhance situational awareness in power systems, in coordination with the existing high-cost high-voltage utility-scale power system monitoring equipment. If the locations and parameters of the utility assets are known, one may expand the analysis to even identify the root causes of the detected malfunctions.

## References


[1] W. Xu, Z. Huang, X. Xie, and C. Li, "Synchronized waveforms – a frontier of data-based power system and apparatus monitoring, protection, and control," *IEEE Trans. on Power Delivery*, vol. 37, no. 1, pp. 3–17, Feb. 2022.

[2] A. F. Bastos, S. Santoso, W. Freitas, and W. Xu, "Synchrowaveform measurement units and applications," in *Proc. of IEEE PESGM*, 2019.

[3] H. Mohsenian-Rad and W. Xu, "Synchro-waveforms: A window to the future of power systems data analytics," *IEEE Power and Energy Magazine*, Apr. 2023.

[4] C. Halliday, "Visualization of real time system dynamics using enhanced monitoring (visor)," in *VISOR: Close Down Report*, Mar 2018.

[5] A. G. Phadke and J. S. Thorp, *Synchronized Phasor Measurements and Their Applications*. Springer, Jan. 2007.

[6] H. Mohsenian-Rad et al., "Synchro-waveform measurements and data analytics in power systems," Dec. 2024, [Online] Available: https://ieee-synchrowaveform.engr.ucr.edu/sites/default/files/2025-06/pes-tr127.pdf.

[7] J. Patterson and A. Pal, "An inductively powered line-mounted time-synchronized micro point-on-wave recorder," in *Proc. of the IEEE PESGM*, Jul. 2021.

[8] A. Shirsat, H. Sun, K. J. Kim, J. Guo, and D. Nikovski, "1 convednet: A convolutional energy disaggregation network using continuous point-on-wave measurements," in *Proc. of the IEEE PESGM*, Jul. 2022.

[9] R. Badawi and B. Lesieutre, "Faults and transients observed in continuous distribution-level point-on-wave data," in *Proc. of IEEE NAPS*, 2024.

[10] H. Yin, W. Qiu, Y. Wu, W. Yu, J. Tan, A. Hoke, C. J. Kruse, B. W. Rockwell, and Y. Liu, "Anomaly identification of synchronized voltage waveform for situational awareness of low inertia systems," *IEEE Trans. on Smart Grid*, vol. 16, no. 3, pp. 2416–2428, 2025.

[11] S. Xiong, Y. Liu, J. Fang, J. Dai, L. Luo, and X. Jiang, "Incipient fault identification in power distribution systems via human-level concept learning," *IEEE Trans. on Smart Grid*, vol. 11, no. 6, pp. 5239–5248, 2020.

[12] H. Liu, S. Liu, J. Zhao, T. Bi, and X. Yu, "Dual-channel convolutional network-based fault cause identification for active distribution system using realistic waveform measurements," *IEEE Trans. on Smart Grid*, vol. 13, no. 6, pp. 4899–4908, 2022.

[13] Q. Li, H. Luo, H. Cheng, Y. Deng, W. Sun, W. Li, and Z. Liu, "Incipient fault detection in power distribution system: A time–frequency embedded deep-learning-based approach," *IEEE Trans. on Instrumentation and Measurement*, vol. 72, pp. 1–14, 2023.

[14] W. Qiu, H. Yin, Y. Dong, X. Wei, Y. Liu, and W. Yao, "Synchro-waveform-based event identification using multi-task time-frequency transform networks," *IEEE Trans. on Smart Grid*, vol. 16, no. 3, pp. 2647–2658, 2025.

[15] M. Izadi and H. Mohsenian-Rad, "Synchronous waveform measurements to locate transient events and incipient faults in power distribution networks," *IEEE Trans. on Smart Grid*, vol. 12, no. 5, Sep. 2021.

[16] ——, "A synchronized lissajous-based method to detect and classify events in synchro-waveform measurements in power distribution networks," *IEEE Trans. on Smart Grid*, vol. 13, no. 3, pp. 2170–2184, May 2022.

[17] P. Zhang, M. Hou, R. Liang, Z. Tang, J. Li, M. Jin, Z. Sun, and N. Peng, "Incipient fault detection of medium-voltage distribution cable systems using time-frequency analysis of grounding wire currents," *IEEE Trans. on Smart Grid*, vol. 16, no. 1, pp. 74–86, 2025.

[18] K. Mestav, X. Wang, and L. Tong, "A deep learning approach to anomaly sequence detection for high-resolution monitoring of power systems," *IEEE Trans. on Power Systems*, vol. 38, no. 1, pp. 4–13, Jan. 2023.

[19] M. MansourLakouraj, H. Hosseinpour, H. Livani, and M. Benidris, "Waveform measurement unit-based fault location in distribution feeders via short-time matrix pencil method and graph neural network," *IEEE Trans. on Industry Applications*, vol. 59, pp. 2661–2670, Dec. 2023.

[20] J. Li, Z. Teng, Q. Tang, and J. Song, "Detection and classification of power quality disturbances using double resolution s-transform and dag-svms," *IEEE Trans. on Instrumentation and Measurement*, vol. 65, no. 10, pp. 2302–2312, 2016.

[21] L. Fu, K. Yan, and T. Zhu, "Powercog: A practical method for recognizing power quality disturbances accurately in a noisy environment," *IEEE Trans. on Industrial Informatics*, vol. 18, no. 5, pp. 3105–3113, 2022.

[22] Y. Ma, Q. Li, H. Chen, H. Li, and Y. Lei, "Voltage transient disturbance detection based on the rms values of segmented differential waveforms," *IEEE Access*, vol. 9, pp. 144 514–144 529, 2021.

TABLE V
DETAILED SIGN VECTORS AND AUTO-CORRELATION RESULTS FOR VARIOUS CHOICES OF PARAMETER $N$

| $N^{\max}$ | Variations of $\mathrm{SGN}_{\Delta v}$ | $\mathrm{AC}_{\Delta v}$ = Auto-Correlation $\{\mathrm{SGN}_{\Delta v}\}$ | $P$ |
|---|---|---|---|
| 5 | $[+1\ -1\ +1\ -1\ +1]$ | $[+1.0 \vdots -0.80\ \mathbf{+0.60}\ -0.40\ +0.20]$ | 2 |
| 6 | $[+1\ -1\ +1\ -1\ +1\ -1]$ | $[+1.0 \vdots -0.83\ \mathbf{+0.67}\ -0.50\ +0.33\ -0.17]$ | 2 |
| | $[+1\ -1\ +1\ -1\ +1\ +1]$ | $[+1.0 \vdots -0.50\ \mathbf{+0.33}\ -0.17\ +0.00\ +0.17]$ | |
| 7 | $[+1\ -1\ +1\ -1\ +1\ -1\ +1]$ | $[+1.0 \vdots -0.86\ \mathbf{+0.71}\ -0.57\ +0.43\ -0.29\ +0.14]$ | 2 |
| | $[+1\ -1\ +1\ -1\ +1\ +1\ +1]$ | $[+1.0 \vdots -0.29\ \mathbf{+0.43}\ -0.29\ +0.14\ +0.00\ +0.14]$ | |
| 8 | $[+1\ -1\ +1\ -1\ +1\ -1\ +1\ -1]$ | $[+1.0 \vdots -0.88\ \mathbf{+0.75}\ -0.62\ +0.50\ -0.38\ +0.25\ -0.12]$ | 2 |
| | $[+1\ -1\ +1\ -1\ +1\ -1\ +1\ +1]$ | $[+1.0 \vdots -0.62\ \mathbf{+0.50}\ -0.38\ +0.25\ -0.13\ +0.00\ +0.12]$ | |
| | $[-1\ -1\ +1\ -1\ +1\ -1\ +1\ +1]$ | $[+1.0 \vdots -0.38\ \mathbf{+0.25}\ -0.13\ +0.00\ +0.13\ -0.25\ -0.12]$ | |
| 9 | $[+1\ -1\ +1\ -1\ +1\ -1\ +1\ -1\ +1]$ | $[+1.0 \vdots -0.89\ \mathbf{+0.78}\ -0.67\ +0.56\ -0.44\ +0.33\ -0.22\ +0.11]$ | 2 |
| | $[+1\ -1\ +1\ -1\ +1\ -1\ +1\ +1\ +1]$ | $[+1.0 \vdots -0.44\ \mathbf{+0.56}\ -0.44\ +0.33\ -0.22\ +0.11\ +0.00\ +0.11]$ | |
| | $[-1\ -1\ +1\ -1\ +1\ -1\ +1\ +1\ +1]$ | $[+1.0 \vdots -0.22\ \mathbf{+0.33}\ -0.22\ +0.11\ +0.00\ -0.11\ -0.22\ -0.11]$ | |
| | $[-1\ -1\ -1\ -1\ +1\ -1\ +1\ +1\ +1]$ | $[+1.0 \vdots +0.22\ \mathbf{+0.33}\ +0.00\ -0.11\ -0.22\ -0.33\ -0.22\ -0.11]$ | |
| | $[+1\ -1\ -1\ -1\ +1\ -1\ +1\ +1\ +1]$ | $[+1.0 \vdots +0.00\ \mathbf{+0.11}\ -0.22\ +0.11\ -0.44\ -0.11\ +0.00\ +0.11]$ | |
| 10 | $[+1\ -1\ +1\ -1\ +1\ -1\ +1\ -1\ +1\ -1]$ | $[+1.0 \vdots -0.90\ \mathbf{+0.80}\ -0.70\ +0.60\ -0.50\ +0.40\ -0.30\ +0.20\ -0.10]$ | 2 |
| | $[+1\ -1\ +1\ -1\ +1\ -1\ +1\ -1\ +1\ +1]$ | $[+1.0 \vdots -0.70\ \mathbf{+0.60}\ -0.50\ +0.40\ -0.30\ +0.20\ -0.10\ +0.00\ +0.10]$ | |
| | $[+1\ -1\ +1\ -1\ +1\ -1\ +1\ +1\ +1\ +1]$ | $[+1.0 \vdots -0.30\ \mathbf{+0.60}\ -0.30\ +0.20\ -0.10\ +0.00\ +0.10\ +0.00\ +0.10]$ | |
| | $[-1\ -1\ +1\ -1\ +1\ -1\ +1\ +1\ +1\ +1]$ | $[+1.0 \vdots -0.10\ \mathbf{+0.40}\ -0.10\ +0.00\ +0.10\ -0.20\ -0.10\ -0.20\ -0.10]$ | |
| | $[-1\ -1\ -1\ -1\ +1\ -1\ +1\ +1\ +1\ +1]$ | $[+1.0 \vdots +0.30\ \mathbf{+0.40}\ +0.10\ -0.20\ -0.10\ -0.40\ -0.30\ -0.20\ -0.10]$ | |
| | $[+1\ -1\ -1\ -1\ +1\ -1\ +1\ +1\ +1\ +1]$ | $[+1.0 \vdots -0.10\ \mathbf{+0.40}\ -0.10\ +0.00\ +0.10\ -0.20\ -0.10\ -0.20\ -0.10]$ | |


[23] M. F. Al-Mashdali et al., “Signal processing-free intelligent model for power quality disturbances identification,” *IEEE Access*, vol. 13, pp. 9910–9922, 2025.

[24] A. Shahsavari, M. Farajollahiand E. Stewartand E. Cortez, and H. Mohsenian-Rad, “Situational awareness in distribution grid using micro-pmu data: A machine learning approach,” *IEEE Trans. on Smart Grid*, vol. 10, no. 6, pp. 6167–6177, Jul. 2019.

[25] S. S. Negi, N. Kishor, K. Uhlen, and R. Negi, “Event detection and its signal characterization in pmu data stream,” *IEEE Trans. on Industrial Informatics*, vol. 13, no. 6, pp. 3108–3118, Dec. 2017.

[26] N. T. Bazargani, G. Dasarathy, L. Sankar, and O. Kosut, “A machine learning framework for event identification via modal analysis of pmu data,” *IEEE Trans. on Power Systems*, vol. 38, no. 5, Oct. 2023.

[27] N. Ehsani, F. Aminifar, and H. Mohsenian-Rad, “Convolutional autoencoder anomaly detection and classification based on distribution pmu measurements,” *IET Generation, Transmission, and Distribution*, vol. 16, no. 14, pp. 2816–2828, Jul. 2022.

[28] T. Wu, Y.-J. Angela Zhang, and X. Tang, “Online detection of events with low-quality synchrophasor measurements based on $i$forest,” *IEEE Trans. on Industrial Informatics*, vol. 17, no. 1, pp. 168–178, Jan 2021.

[29] A. Silverstein and J. Follum, “High-resolution, time-synchronized grid monitoring devices,” in *Proc. of the NASPI Technical Report*, Mar. 2020.

[30] J.D. Follum et al., “Advanced measurements for resilient integration of inverter-based resources: Progress matrix year-1 report,” PNNL Report, Mar. 2023.

[31] C. Guarnieri Calò Carducci, M. Pau, C. Cazal, F. Ponci, and A. Monti, “Smu open-source platform for synchronized measurements,” *Sensors*, vol. 22, no. 14, Jul. 2022.

[32] F. Rahmatian, “Impact of data quality on synchro- waveform data analytics,” *Presented at the IEEE PESGM (Panel)*, Jul. 2023.

[33] W. Qiu, H. Yin, Y. Wu, C. Chen, L. Zhan, C. Zeng, and Y. Liu, “Synchro-waveform data compression using multi-stage hybrid coding algorithm,” *Measurement*, vol. 232, p. 114709, 2024.

[34] D. Laverty, M. Rusch, D. Saba, and A. Von Meier, “Open source time synchronised sampled value logger for power system studies,” in *Proc. of the ISSC*, Jul. 2022.

[35] X. Jiang, B. Stephen, and S. McArthur, “A sequential bayesian approach to online power quality anomaly segmentation,” *IEEE Trans. on Industrial Informatics*, vol. 17, no. 4, pp. 2675–2685, Apr 2021.

[36] B. Gao, R. Torquato, W. Xu, and W. Freitas, “Waveform-based method for fast and accurate identification of subsynchronous resonance events,” *IEEE Trans. on Power System*, vol. 34, no. 5, pp. 3626–3636, Sep. 2019.

[37] Y. Cheng et al., “Real-world subsynchronous oscillation events in power grids with high penetrations of inverter-based resources,” *IEEE Trans. on Power Systems*, vol. 38, no. 1, pp. 316–330, Jan. 2023.

[38] W. Xu, J. Yong, H. J. Marquez and C. Li, “Interharmonic power – a new concept for power system oscillation source location,” *IEEE Trans. on Power Systems*, vol. early access, pp. 1–13, 2025.

[39] P. Kuwałek, A. Bracale, T. Sikorski, and J. Rezmer, “Synchronized approach based on empirical fourier decomposition for accurate assessment of harmonics and specific supraharmonics,” *IEEE Trans. on Industrial Electronics*, vol. 72, no. 1, pp. 992–1002, Jan. 2025.

[40] H. Mohsenian-Rad, A. Shahsavari, and M. Majidi, “Analysis of power quality events for wildfire monitoring: Lessons learned from a california wildfire,” in *Proc. of the IEEE PES ISGT*, Nov. 2023.

[41] J. Y. Joo et al., “Detecting anomalies for fire prevention in distribution systems: Challenges and analytical techniques,” *IEEE Power and Energy Magazine*, vol. 22, no. 6, pp. 83–90, Nov 2024.

[42] A. Karpilow, M. Paolone, A. Derviškadić, and G. Frigo, “Step change detection for improved rocof evaluation of power system waveforms,” in *Proc. of the SGSMA*, May 2022.

[43] L. Chen, X. Xie, J. He, T. Xu, D. Xu, and N. Ma, “Wideband oscillation monitoring in power systems with high-penetration of renewable energy sources and power electronics: A review,” *Renewable and Sustainable Energy Reviews*, vol. 175, Apr 2023.

[44] A. Karpilow, A. Derviškadić, G. Frigo, and M. Paolone, “Characterization of non-stationary signals in electric grids: A functional dictionary approach,” *IEEE Trans. on Power Systems*, vol. 37, no. 2, pp. 1126–1138, Mar. 2022.

[45] A. McEachern, “Gridsweep - new instrument for grid stability research,” *NASPI Working Group Meeting*, Oct. 2022.

[46] GridSweep Synchro-waveform Dataset, *IEEE Task Force on Big Data Analytics for Synchro-Waveform Measurements*, https://ieee-synchrowaveform.engr.ucr.edu/data-sets.

[47] “IEEE Standard 519-2014: Recommended Practice and Requirements for Harmonic Control in Electric Power Systems,” 2014.

[48] H. Mohsenian-Rad, *Smart Grid Sensors: Principles and Applications*. Cambridge University Press, UK, Apr. 2022.

[49] M. Müller, *Information retrieval for music and motion*. Springer, 2007.

[50] J. A. Hartigan and M. A. Wong, “Algorithm as 136: A k-means clustering algorithm,” *Journal of the Royal Statistical Society. Series C (Applied Statistics)*, vol. 28, no. 1, pp. 100–108, 1979.

[51] A. McEachern, “Waveform apparatus disturbance detection and method,” U.S. Patent 4,694,402, filed 1985, expired 2009.

[52] [Online]. Available: https://mathworks.com/help/econ/autocorr.html.